Numerical-experimental approach to identify the effect of relative humidity on the material parameters of a rate-dependent damage model for polyamide 66

Soheil Satouri[a], Rabii Chekkour[a], George Chatzigeorgiou[a], Fodil Meraghni[a*], Gilles Robert[b]

[a] *Arts et Métiers Institute of Technology, CNRS, Université de Lorraine, LEM3-UMR 7239, F-57000, Metz, France*

[b] *DOMO Chemicals – Polytechnyl SAS, Usine de Belle Etoile, 69190 Saint-Fons, France*

Abstract

This work aims at identifying the behavior of polyamide 66 (PA66) under different Relative Humidity (RH) conditions using a phenomenological model that accounts for viscoelastic and viscoplastic rheology coupled to ductile damage. An experimental approach is designed considering different loading conditions, namely: monotonic at several strain rates, loading-unloading, creep-recovery, and cyclic tests. These experiments are chosen to discriminate the various active mechanisms governing the nonlinear behavior of PA66. The thermodynamic background of the phenomenological model, the evolution laws, and the accompanying RH-dependent material parameters are presented and discussed. Using the experimental findings, an optimization algorithm is adopted to identify the model parameters. The latter are investigated with regard to the relative humidity, leading hence to the development of a model that accounts for the effect of RH on all inelastic mechanisms and ductile damage. Validation through experimental data for RH=0%, 25%, 50%, 65%, and 80% reveals that the current model captures the effect of RH and yields mechanical responses in good agreement with experimental findings, notably at higher RH levels. The current numerical-experimental framework presents a unified model for a wide range of humidity conditions and provides a better insight into material properties and rate-dependent inelastic mechanisms under humidity exposure, which typical models do not provide. In addition, the present constitutive law is easily adoptable in micromechanics schemes for the study of polymer based composite materials and structures.

Keywords: Relative Humidity (RH), experimental identification, polyamide 66, viscoelasticity,

*Corresponding author
Email address: fodil.meraghni@ensam.eu (Fodil Meraghni[a])

viscoplasticity, ductile damage.

1. Introduction

Polyamide 66 is one of the most popular and widely used polymers in various industries, such as the automotive, aerospace, and energy industries, thanks to its compatible mechanical properties and low cost of production. In the automotive industry, glass reinforced polyamides can be used in clutch pedals, seat frames, door structures, cooling fans, air filter nozzles, etc. (Pivdiablyk et al., 2020; Obeid, 2016). This wide range of applications is accompanied by a variety of environmental conditions, of which moisture is of great importance. Variation in the material water content leads to changes in the mechanical behavior from glassy to rubbery. With this in mind, predicting the mechanical response of polyamide 66 using numerical models depending on the water uptake level is an important challenge in the industry. Polyamide 66 is often used in industry in the form of glass-reinforced composites. Studying the moisture effect on composites by considering nonlinear inelastic mechanisms and ductile damage can be quite challenging using a multiscale framework. Therefore, in this research, an attempt was made to study polyamide 66 by itself, for which the resulting framework can be integrated into a composite model later. It should be noted that in composites, since glass fibers do not allow for large deformations before failure, the model is based on small deformation theory.

Polyamides have amide groups in their chemical structure that allow them to absorb water up to their saturation limit, depending on the temperature. Many studies have investigated the reversible and irreversible reactions that occur in polyamides due to water absorption and their effect on properties (Kauffman, 1988; Brydson, 1999; Venoor et al., 2021).Water content has an inverse relationship with the glass transition temperature of polyamides and, to some extent, polysulfones, and its increase can cause the glass transition temperature to drop below room temperature, resulting in a change in physical properties such as Young's modulus and yield strength (Apinis et al., 1975; Reimschuessel, 1978; Pramoda and Liu, 2004; Ishisaka et al., 2004; Bellenger et al., 2006; Broudin et al., 2015; Le Gac et al., 2017; Obeid et al., 2018; Venoor et al., 2021). This has been reported as the "water-induced plasticizing" effect in the literature (Sambale et al., 2019; Venoor et al., 2021). In other words, the behavior of the material can change from glass-like to rubber-like at room temperature due to the change in the glass transition temperature. The plasticizing effect

also amplifies inelastic mechanical responses, in which plasticity plays a more important role in the damage mechanism.

To model the diffusion of moisture in polyamide 66, the Fickian and non-Fickian models are employed. According to Fick's law, the rate of diffusion is proportional to the water concentration gradient in the material and the diffusion process is completely reversible. However, non-Fickian diffusion does not follow either of these assumptions (Post et al., 2009). Zhang et al.(Zhang et al., 2015) studied the effect of temperature-humidity coupling on the diffusion process. Although polymers often exhibit non-Fickian diffusion behavior, they used the Fickian diffusion model by considering short-term moisture exposure. Parodi et al. (Parodi et al., 2018) conducted an experimental study to explore the effect of moisture and temperature on the mechanical responses and glass transition temperatures of polyamide 6, and they modified the Ree-Eyring equation by including the glass transition temperature to predict the yield strength and plastic strain rate at different moisture levels. Vidinha et al. (Vidinha et al., 2022) presented a numerical model to predict the mechanical responses of glass/epoxy composites exposed to seawater by considering humidity induced damage. They modeled damage by the degradation of lamina strength as a function of water concentration based on the Fick's law. As mentioned, many attempts have been made to predict the effect of moisture on the behavior of polymer composites. However, for polyamide 66, depending on the water content, time-dependent nonlinear inelastic mechanisms must also be considered. This leads to complexity when incorporating Fickian or non-Fickian models to capture the effect of RH on the active mechanisms. Accordingly, here, as another approach, the model parameters can be obtained as functions of relative humidity through a numerical-experimental framework. In this respect, it is necessary to ensure that all active mechanisms that determine the mechanical behavior of the polyamide are carefully considered. In the following, the polyamide 66 active mechanisms and the available rheological models are briefly discussed.

Considering the importance of environmental effects, the rheological properties and dominant mechanisms of polymers and composites in different hygro-thermo-mechanical conditions have been investigated experimentally in many studies (Arruda et al., 1995; Bergeret et al., 2001; Carrascal et al., 2005; Arif et al., 2014a,b), and many constitutive laws have been presented in the literature (Arruda and Boyce, 1993; Launay et al., 2011; Billon, 2012; Krairi and Doghri, 2014; Praud et al., 2017; Benaarbia et al., 2018a). Polymers exhibit inelastic nonlinear behavior which has been reported as viscoelastic viscoplastic mechanisms in the literature through creep-recovery experiments

(Arif et al., 2014a; Benaarbia et al., 2014, 2016, 2019). Models that have been proposed to capture their nonlinear behavior are mainly developed through macro-molecular network-based (Arruda and Boyce, 1993; Billon, 2012) and phenomenological approaches (Launay et al., 2011; Krairi and Doghri, 2014; Praud et al., 2017; Benaarbia et al., 2018a). The constitutive models considering macro-molecular network-based frameworks require the physical data that are not easily obtainable through experimental measurements. On the contrary, phenomenological models based on thermodynamic principles use material parameters that can be identified through standard mechanical tests.

Viscoelastic models of polymers are generally formulated through two major approaches: integral form and differential form representations (Miled et al., 2011; Krairi and Doghri, 2014). The integral representation requires the integration of the entire time history to describe the stress-strain relation. Green, Rivlin, and Spencer (Rivlin, 1983), Pipkin and Rogers (Pipkin and Rogers, 1968) are some examples of them. On the other hand, differential representation proposes the linear viscoelastic models, such as Maxwell, Kelvin-Voigt, Burgers, and their extensions, which are modeled using rheological elements as linear springs and dashpots. This approach allows simulating the viscoelastic mechanism using some viscoelastic state variables and their corresponding parameters.

The modeling approaches for plasticity are categorized in unified and non-unified theories (Chaboche and Rousselier, 1983; Contesti and Cailletaud, 1989). In the unified theory, the plasticity and creep (i.e. viscosity) are considered as a single rate dependent inelastic variable in the constitutive model (Chaboche, 2008; Barrett et al., 2013). However, the non-unified theory proposes two separate variables for plasticity and creep which are rate independent and rate dependent respectively (Cailletaud and Sai, 1995; Velay et al., 2006). Using the non-unified theory is efficient when the creep is dominant, which normally occurs at high temperatures (Kang and Kan, 2007). However, difficulties in finite element implementation have been reported for the models using non-unified theories (Benaarbia et al., 2018b).

In this paper, the inelastic behavior of polyamide 66 is modeled through a viscoelastic viscoplastic incremental framework accounting for ductile damage driven by plasticity (VEVPD). This model has been initially developed (Praud et al., 2017) for predicting the behavior of polyamide 66 at constant RH. In this work, the effect of RH on the nonlinear mechanical response is captured by identifying the elastic, inelastic and damage parameters as functions of the RH. To this end, an experimental approach is designed to study the material response under different types of loading

with different rates, then an optimization method is adopted to calibrate the model at different RH using the experimental findings. The novelties of the present work are the formulation of a VEVPD model whose material parameters are RH dependent, as well as the design of an experimental approach leading to descriminate the various active mechanisms governing the nonlinear behavior of PA66. This provides a helpful tool to perform a reliable hygromechanical analysis. It should be noted that the constitutive laws have been developed considering small deformations and rotations and will be implemented in the future in homogenization approaches (full-field and mean-field). This assumption is due to the fact that the PA66 usually appears in applications as matrix phase in composites. The latter cannot exhibit large deformations due to the presence of the reinforcement. With this in mind, it is reasonable to limit the study of PA66 behavior at the small deformations regime.

This paper is organized as follows: in section 2, the model with all the thermodynamical backgrounds and constitutive laws is recalled briefly. In section 3, the experimental protocol is presented and the obtained data are explored. Then, the optimization framework is discussed and the model is calibrated and validated using the experimental results.

2. Theoretical background and numerical modeling

As discussed in the introduction, polyamide 66 exhibits nonlinear and dissipative mechanisms, such as viscoelasticity, viscoplasticity, and ductile damage (Arif et al., 2014b; Benaarbia et al., 2014, 2016; Praud et al., 2017; Benaarbia et al., 2019). Accordingly, the material behavior prediction requires an appropriate thermodynamic framework considering the mentioned dominant mechanisms. Praud et al. (Praud et al., 2017) have presented a phenomenological model and validated the numerical results with the experimental data at RH50. In this study, the parameters of the latter model are identified at different RH levels and validated with experimental data. In this section, the corresponding rheological model and the thermodynamic framework are briefly presented.

2.1. Nonlinear mechanisms in polyamide 66

In this study, the phenomenological model is developed using the Thermodynamics of Irreversible Processes (TIP) (Halphen and Nguyen, 1975; Germain et al., 1983), and a viscoelastic viscoplastic rheological framework is applied to capture the inelastic behavior of the material, in

which the total strain is decomposed into elementary elastic, viscoelastic and viscoplastic components. The viscoelastic mechanism is simulated considering multiple time ranges. To achieve that, here four Kelvin-Voigt branches with different characteristic times are defined to capture viscoelasticity. Unified viscoplasticity theory considering isotropic hardening function is adopted to model the rate dependent plasticity and creep. The viscoplasticity is activated once exceeding the von Mises yield function, f:

$$f = \frac{\sigma^{eq}}{1-D} - R(r) - R_0, \tag{1}$$

where σ^{eq} is the equivalent stress calculated as $\sqrt{\frac{3}{2}\boldsymbol{\sigma'} : \boldsymbol{\sigma'}}$, in which $\boldsymbol{\sigma'}$ stands for the deviatoric part of the stress tensor, and D denotes the ductile damage which is defined as an internal variable to describe stiffness reduction through the well-known effective stress concept (Kachanov, 1958; Rabotnov, 1968; Lemaitre and Chaboche, 1994; Chaboche, 1997). R_0 denotes the elastic limit, and $R(r)$ is the isotropic hardening function:

$$R(r) = H_m\, r^{H_p}, \tag{2}$$

where r is the hardening state variable, and H_m and H_p are the hardening-related model parameters. The viscoplastic model is introduced through a power law formulation, based on which, the hardening state variable rate, $\dot{r}$, is defined as the following function:

$$\dot{r} = \langle \frac{f(\boldsymbol{\sigma}, -R; D, r)}{R_{vp}} \rangle_+^{P_{vp}^{-1}}, \tag{3}$$

where "$\langle\,.\,\rangle_+$" is the Macauley brackets, and R_{vp} and P_{vp} are the viscoplastic resistance and exponent, respectively. The rheological model can be represented by physical components, such as springs and dashpots, as illustrated in Figure 1. As observed, the elastic part is assumed as a single linear spring under the elastic strain, $\boldsymbol{\epsilon}^e$. The i^{th} Kelvin-Voigt branch is described through a linear spring and a linear dashpot subjected to the i^{th} viscoelastic strain, $\boldsymbol{\epsilon}^{vi}$. The viscoplastic branch is considered as an assembly of a nonlinear spring, nonlinear dashpot, and a frictional element, which is subjected to the viscoplastic strain, $\boldsymbol{\epsilon}^{vp}$. In the next subsection, the corresponding constitutive laws are derived based on thermodynamic principles and the present rheological model.

2.2. Constitutive laws

Considering the rheological model introduced in the previous section, the thermodynamic potential is defined as Helmholtz free energy which is divided to elastic, viscoelastic, and viscoplastic

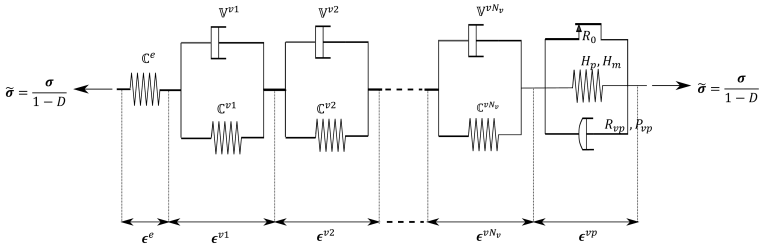

Figure 1: Schematics of the VEVPD rheological modeld. Here, $\tilde{\boldsymbol{\sigma}}$ stands for the second order effective stress tensor.

parts:

$$\Psi(\boldsymbol{\epsilon}, \boldsymbol{\epsilon}^{vi}, \boldsymbol{\epsilon}^{vp}, r, D) = \Psi^e(\boldsymbol{\epsilon}, \boldsymbol{\epsilon}^{vi}, \boldsymbol{\epsilon}^{vp}, D) + \sum_{i=1}^{4} \Psi^{vi}(\boldsymbol{\epsilon}^{vi}, D) + \Psi^{vp}(r), \tag{4}$$

with

$$\Psi^e = \frac{1}{2}\left(\boldsymbol{\epsilon} - \sum_{i=1}^{4} \boldsymbol{\epsilon}^{vi} - \boldsymbol{\epsilon}^{vp}\right) : (1-D)\mathbb{C}^e : \left(\boldsymbol{\epsilon} - \sum_{i=1}^{4} \boldsymbol{\epsilon}^{vi} - \boldsymbol{\epsilon}^{vp}\right), \tag{5a}$$

$$\Psi^{vi} = \frac{1}{2}\boldsymbol{\epsilon}^{vi} : (1-D)\mathbb{C}^{vi} : \boldsymbol{\epsilon}^{vi}, \tag{5b}$$

$$\Psi^{vp} = \int_0^r R(\alpha)\, d\alpha. \tag{5c}$$

where $\mathbb{C}^e$ and $\mathbb{C}^{vi}$ denote the fourth order elastic and i^{th} viscoelastic stiffness tensors, respectively. Considering the thermodynamic function, the state laws are derived as partial derivatives with respect to strain and internal state variables (i.e. $\boldsymbol{\epsilon}^{vi}$, $\boldsymbol{\epsilon}^{vp}$, and r) and are listed in table 1. $\boldsymbol{\sigma}$, $\boldsymbol{\sigma}^{vi}$, R, and Y are the conjugate state variables. Based on the second principle of thermodynamics in the form of Clausius-Duhem inequality, dissipation is always zero or positive and is derived as the difference between the strain and stored energy rates:

$$\mathcal{D} = \boldsymbol{\sigma}\dot{\boldsymbol{\epsilon}} - \dot{\Psi} \geq 0, \tag{6}$$

where it is expanded as:

$$\mathcal{D} = \boldsymbol{\sigma}\dot{\boldsymbol{\epsilon}} - \left(\frac{\partial \Psi}{\partial \boldsymbol{\epsilon}} : \dot{\boldsymbol{\epsilon}} + \frac{\partial \Psi}{\partial \boldsymbol{\epsilon}^{vp}} : \dot{\boldsymbol{\epsilon}}^{vp} + \sum_{i=1}^{4} \frac{\partial \Psi}{\partial \boldsymbol{\epsilon}^{vi}} : \dot{\boldsymbol{\epsilon}}^{vi} + \frac{\partial \Psi}{\partial r} : \dot{r} + \frac{\partial \Psi}{\partial D} : \dot{D}\right) \geq 0, \tag{7}$$

and reduced to:

$$\mathcal{D} = \sum_{i=1}^{4} \boldsymbol{\sigma}^{vi} : \dot{\boldsymbol{\epsilon}}^{vi} + \boldsymbol{\sigma} : \dot{\boldsymbol{\epsilon}}^{vp} - R\dot{r} + Y\dot{D} \geq 0. \tag{8}$$

Viscoelastic elementary components rates, $\dot{\boldsymbol{\epsilon}}^{vi}$, are derived by partial derivatives with respect to their related thermodynamic forces using the set of potentials, Ω^{vi}, which are defined as:

$$\Omega^{vi} = \frac{1}{2}\boldsymbol{\sigma}^{vi} : \frac{\mathbb{V}^{vi^{-1}}}{1-D} : \boldsymbol{\sigma}^{vi}, \tag{9}$$

where $\mathbb{V}^{vi}$ is the viscosity tensor corresponding to the i^{th} Kelvin-Voigt branch, and $\boldsymbol{\sigma}^{vi}$ is the second order tensor of viscoelastic conjugate state variable. Also, the J_2-viscoplasticity theory (Chaboche, 1997) is adopted to derive viscoplastic strain rate by defining the identification function, F:

$$F = f + f_D, \quad \text{with} \quad f_D = \frac{S_D}{(\beta_D+1)(1-D)}\left(\frac{Y}{S_D}\right)^{\beta_D+1}, \tag{10}$$

Where S_D and β_D are the model parameters controlling the damage growth, and Y denotes the damage conjugate state variable. The latter model has been used primarily for ductile damage in metals, in which the damage grows slowly in the beginning and very rapidly in the final stages of loading. However, the damage progression is different in polymers, for whom the damage initiation is quite rapid at the beginning and then slowly grows thereafter (Detrez et al., 2011). For metals, the sign of β_D is positive yielding increasing damage rate with respect to plasticity. However, for polymers, the damage behavior can be captured by considering negative sign for β_D (Krairi and Doghri, 2014). Considering the negative β_D in the present model, the damage-related function, f_D, can be negative if β_D is smaller than -1, but the dissipation sign is not affected and the dissipation stays zero or positive (Chen et al., 2023). In other words, thermodynamically speaking, there is no restriction about the sign of F as long as the mechanical dissipation stays zero or positive according to Clausius-Duhem inequality.

The evolution laws of the present VEVPD model are derived using the dual potential and identification functions defined earlier and listed in Table 1. For the sake of brevity, the full formulation and demonstrations are not expressed here, but further details along with the numerical implementation can be studied at (Praud et al., 2017).

As discussed in the introduction, the influence of material moisture on nonlinear inelastic mechanisms and ductile damage must also be included in the phenomenological framework. To this end, there are two different approaches: i) using new parameters through Fickian and non-Fickian diffusion models (Wang et al., 2016; Arhant et al., 2016), ii) using the model parameters as a function of RH. In the present study, the second option is adopted and the parameters are determined for different relative humidity levels. These parameters can be divided into elastic, viscoelastic, viscoplastic, and damage-related, listed in the Table 2.

Table 1: State and evolution laws for the viscoelastic viscoplastic material (Praud et al., 2017) (λ, $\mathbf{\Lambda}_{vp}$, and Λ_D are viscoplastic multiplier, plastic flow, and damage direction respectively.)

State variable	Conjugate variable	Evolution laws
strain tensor, $\boldsymbol{\epsilon}$	$\boldsymbol{\sigma}=\dfrac{\partial \Psi}{\partial \boldsymbol{\epsilon}}$	-
Viscoelastic strains, $\boldsymbol{\epsilon}^{vi}$	$-\boldsymbol{\sigma}^{vi} = \dfrac{\partial \Psi}{\partial \boldsymbol{\epsilon}^{vi}}$ $= (1-D)\mathbb{C}^{vi} : \boldsymbol{\epsilon}^{vi} - \boldsymbol{\sigma}$	$\dot{\boldsymbol{\epsilon}^{vi}} = \dfrac{\partial \Omega^{vi}}{\partial \boldsymbol{\sigma}^{vi}} = \dfrac{(\mathbb{V}^{vi})^{-1}}{1-D} : \boldsymbol{\sigma}^{vi}$
Viscoplastic strain, $\boldsymbol{\epsilon}^{vp}$	$-\boldsymbol{\sigma} = \dfrac{\partial \Psi}{\partial \boldsymbol{\epsilon}^{vp}}$	$\dot{\boldsymbol{\epsilon}^{vp}} = \dfrac{\partial F}{\partial \boldsymbol{\sigma}}\dot{\lambda} = \Lambda_{vp}\dot{\lambda}$
Hardening state variable,r	$R = \dfrac{\partial \Psi}{\partial r}$ $R = H_m\, r^{H_p}$	$\dot{r} = \dot{\lambda}$
Damage, D	$-Y = \dfrac{\partial \Psi}{\partial D}$	$\dot{D} = \dfrac{\partial F}{\partial Y}\dfrac{\dot{\lambda}}{1-D} = \Lambda_D \dot{\lambda}$

Table 2: RH dependent parameters of the VEVPD model that need to be identified through suitable experimental approach.

Mechanism	Parameters
Elastic	E
Viscoelastic	$\{E^{vi},\, \eta^{vi},\, \tau^{vi}\}_{i=1,4}$
Viscoplastic	$H_m,\, H_p,\, R_{vp},\, P_{vp}$
Damage	$S_D,\, \beta_D$

3. Calibration and validation of the VEVPD model against experimental results

As mentioned before, polyamide 66 exhibits different mechanisms depending on the environmental conditions. The behavior of semi-crystalline polymers with the glass transition temperature T_g and at the temperature T can be classified through the glass transition criterion $(T - T_g)$. Accordingly, for $T - T_g < 0$, the material shows mostly glassy response, whereas for $T - T_g > 0$ it exhibits viscoelastic rubbery-like state. However, when $T - T_g \approx 0$, the material demonstrates viscoelastic (time-dependent) response. These effects considering the latter criterion are schematically illustrated in the Figure 2. Furthermore, the relation between glass transition temperature and relative humidity is illustrated in Figure 3. Such tendency has also been reported in the literature by Launay et al. (2013). In this view, it becomes clear that the RH impacts the glass transition temperature, which in turn affects the overall response of polyamide. Consequently, the proposed model should be able to predict the different types of rheological response with regard to the RH through proper choice of the material parameters. Thus, the VEVPD model, presented in the previous section, requires to be calibrated through mechanical tests at different RH levels. In the following sections, the methodology and experimental setup is expressed in detail.

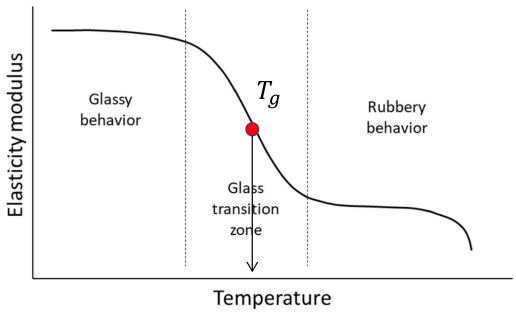

Figure 2: Material behavior state versus the temperature and the glass transition criterion (schematic representation).

3.1. Model parameters identification strategy

A proper experimental approach is designed to capture all mechanisms and identify the related parameters at different RH, namely RH0%, RH25%, RH50%, RH65%, and RH80%. To investigate the effect of RH, considering the correlation between the viscoelastic parameters, the model parameters must be identified in constant viscoelastic characteristic times, τ^{vi}. Here, four viscoelastic

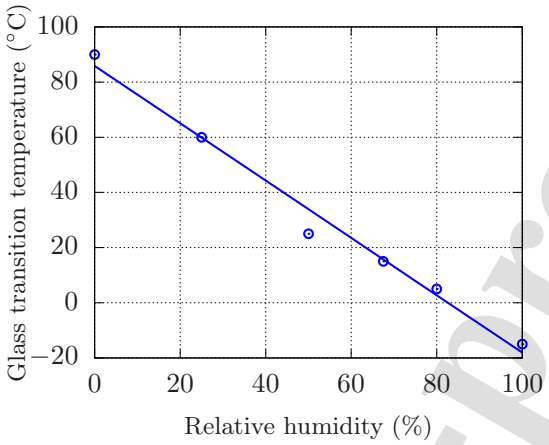

Figure 3: Variation of glass transition temperature of PA66 versus RH estimated through Dynamic Mechanical Analysis (DMA) tests.

branches are considered with constant characteristic times of 0.8 s, 8 s, 80 s, and 800 s. This assumption allows comparing the effect of RH on the viscoelastic moduli, E^{vi}. The viscoelastic modulus, E^{vi}, the characteristic time, τ^{vi}, and the viscosity, η^{vi}, for the i^{th} branch, are related to each other through $\tau^{vi} = \eta^{vi}/E^{vi}$. This means η^{vi} is derived automatically using the other two parameters, E^{vi} and τ^{vi}.

For the model calibration, it is sufficient to define a cost function, $C^r(p)$, between the numerical and experimental responses:

$$C^r(p) = \sum_{k=1}^{N_p} w_k \left[\frac{m_k^{\text{num}}(p) - m_k^{\text{exp}}}{m_k^{\text{exp}}} \right]^2 , \tag{11}$$

where p is the parameters values set, N_p denotes the number of data, m_k^{num} and m_k^{exp} are the numerical and experimental quantities that have to be compared, respectively, and w_k is their corresponding weight in the k^{th} point. To minimize the cost function, Nelder-Mead approach (Nelder and Mead, 1965), which is briefly described in section 3.4, is used as the optimization algorithm. In what follows, the designed experimental process is first described, then the model calibration strategy and methodology are introduced in detail.

3.2. Experimental setup and procedure

3.2.1. Materials and sample preparation

The material used in this study is polyamide 66 supplied by DOMO Chemicals, which commercially known as A218 BK. To perform mechanical tensile tests, dog bone samples are cut using water jet hyperbar machining process, with the dog bone shape and dimensions shown in Figure 4. In order to control the water uptake ratio, the samples are placed in a conditioning chamber at

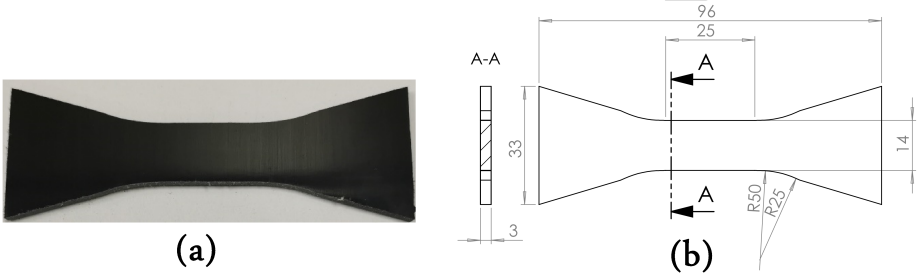

Figure 4: a) Dog bone sample; b) sample schematics and the corresponding dimensions (in mm).

the temperature of 80 °C under dry environment to extract any residual humidity from the samples machining process. Figure 5 shows water desorption with respect to the square root of time, in which a mass reduction is observed until its stabilization. The water content eventually gets around 0.3% (as the residual value).

To recondition at different RH, the samples are placed in the hygrometric chamber, Memmert HCP246 (Figure 6), at the corresponding temperature and humidity. The appropriate temperature and humidity are adjusted depending on the target RH and is performed in two phases: first, the rapid water absorption with a higher conditioning temperature and RH to accelerate the water uptake process, and second, stabilization and homogenization of the humidity along the thickness of the sample to avoid any humidity concentration gradient, during which the temperature is reduced as close as possible to the ambient temperature and the considered RH. Different mass measurements are performed through the conditioning in order to verify the relative humidity evolution. The targeted RH is reached once the mass evolution is constant. Mass measurements are performed using a weighing device with a resolution of 0.1 mg. As an example, the mass with respect to square root of time during the conditioning process at RH65 is plotted and depicted in Figure

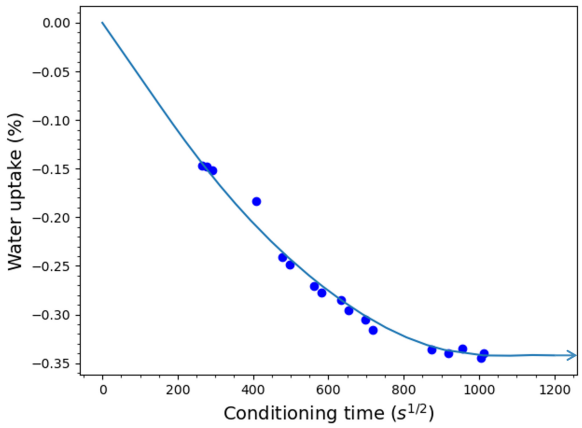

Figure 5: Water loss of the samples with respect to square root of time in the initial drying procedure.

7. The conditioned samples are kept in hermetic envelopes to keep their water content constant. This also prevents undesirable thermomechanical effects by ensuring that the samples are at room temperature before the test.

(a) **(b)**

Figure 6: a) Hygrometric chamber, Memmert HCP246; b) dog bone samples in the hygrometric chamber.

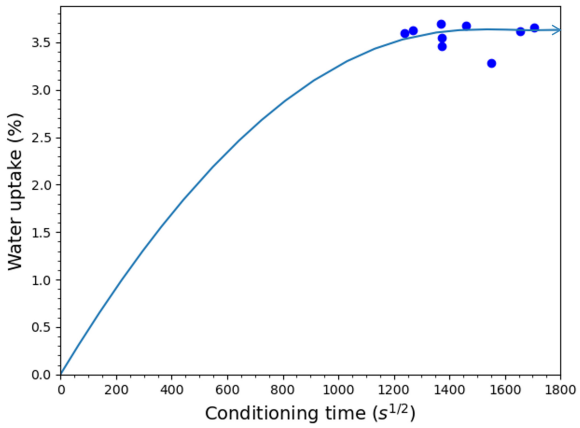

Figure 7: sample mass versus square root of time during water absorption for conditioning at RH65.

3.2.2. Mechanical tests

To calibrate and validate the model, several mechanical tests are performed to capture the dominant mechanisms properly. To this end, time-dependent mechanisms are captured by monotonic tensile tests carried out at three different displacement rates. The evolution of plasticity-induced ductile damage is identified using the loading-unloading test, and the viscoelastic and viscoplastic mechanisms are captured by creep-recovery tests with two different stages of loading at 50 % and 70 % of the ultimate force, F_{ult}, previously determined by monotonic tests. The load is held for 5 min in the creep phase and 5 min in the recovery phase. Figure 8 shows the schematic diagrams of the above mechanical tests used in the calibration procedure. Model parameters identification is performed in several steps. In each step, the model parameters are identified and then used as the initial values for the next step. In each step, experimental data are used as follows:

- 1st step: monotonic loading tests.
- 2nd step: monotonic loading tests and loading-unloading test.
- 3th step: monotonic loading tests, loading-unloading test, and creep-recovery test at 50 % of F_{ult}.
- 4th step: monotonic loading tests, loading-unloading test, creep-recovery test at 50 % of F_{ult}, and creep-recovery test at 70 % of F_{ult}.

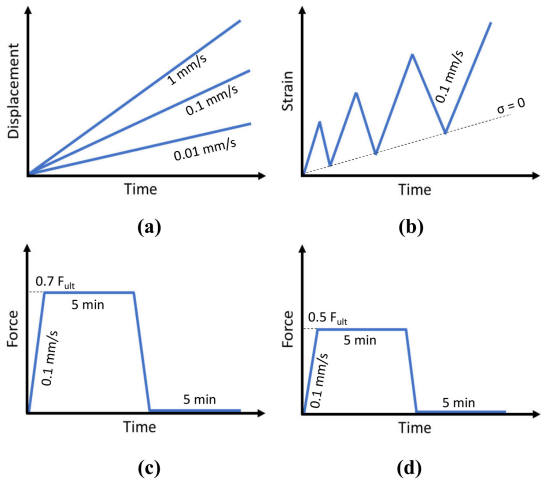

Figure 8: Schematics of the mechanical tests of the calibration phase: a) monotonic displacement-controlled tests, b) loading-unloading test with increasing displacement, c) creep-recovery test with 70 % of F_{ult}, d) creep-recovery test with 50 % of F_{ult}.

The rest of experimental data are considered for the calibrated model validation. Figure 9 shows the schematic diagrams of the mechanical tests used in the validation phase. For implementing the above mechanical tests, the zwick-roell Z050, 50kN machine is employed. To obtain more accurate experimental data, a sample setting tool is designed to ensure the dog bone sample is aligned with the loading axes and avoid any torsional moment (Figure 10). Obviously, this tool is removed before the actual test initiation. The displacement is measured using an extensometer with the gauge length of 25 mm (Figure 11), based on which the corresponding strain is calculated. It should be mentioned that engineering stress and strain are considered here. The stress is calculated based on the original cross-section, and the strain is the displacement of the material per unit length.

Since there are often some slight dimensional errors in the production process of polyamide plates and cutting into dog bone samples, the corresponding cross-section is measured for each sample. The considered mechanical tests are listed in summary as Table 3, in which monotonic, loading-unloading, and creep-recovery tests are abbreviated as "MT", "L-U", and "C-R", respectively.

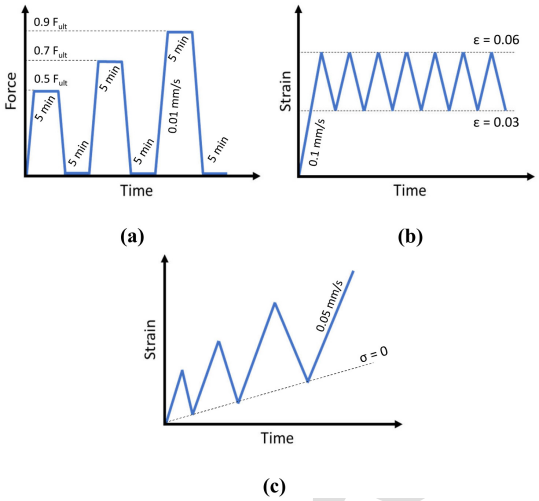

Figure 9: Schematics of the mechanical tests of the validation phase: a) creep-recovery test at different steps, b) cyclic tensile-tensile test, c) loading-unloading test with increasing displacement.

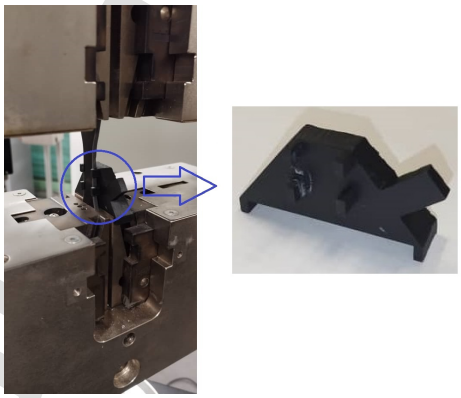

Figure 10: Sample setting tool for keeping the sample aligned with the loading axes.

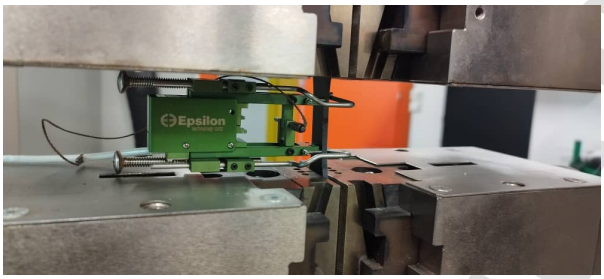

Figure 11: Measurement of displacement of dog bone samples using extensometer.

Table 3: Mechanical tests for the calibration and validation phases.

RH (%)	Calibration phase		Validation phase	
	Test	Loading rate ($mm\,s^{-1}$)	Test	Loading rate ($mm\,s^{-1}$)
0, 25, 50, 65, 80	MT	0.01, 0.1, and 1	Cyclic	0.1
	L-U	0.1	L-U	0.05
	C-R	0.1	C-R	0.01

3.3. Experimental observations

In this subsection, the data obtained through the mechanical tests are studied, and the effect of loading rate and RH are investigated. The monotonic tests are performed in $0.01\,\mathrm{mm\,s^{-1}}$, $0.1\,\mathrm{mm\,s^{-1}}$, and $1\,\mathrm{mm\,s^{-1}}$ displacement rates ($4\times10^{-4}\,\mathrm{s^{-1}}$, $4\times10^{-3}\,\mathrm{s^{-1}}$, and $4\times10^{-2}\,\mathrm{s^{-1}}$ strain rates considering 25 mm gauge length), and the corresponding stress-strain curves are displayed in Figures 12 to 14. As observed, the increase in RH leads to a decrease in the stress level, and the material becomes softer, which confirms the notions in the previous sections about the impact of RH on T_g (plasticization mechanism due to the increase of the water content). In other words, the material exhibits glassy behavior at RH0 and RH25 when $T-T_g<0$, viscoelastic behavior for RH50 ($T-T_g\approx0$) and viscoelastic mostly rubbery response at RH65 and RH80 when $T-T_g>0$. Considering the ambient room temperature at $T=25^oC$ and the glass transition temperatures given in Figure 3, the behavior of polyamide versus glass transition temperature and relative humidity is roughly estimated as table 4. Moreover, the rate dependent mechanical response of the material yields higher stress level for faster loading rates (Figures 12 to 14). Creep-recovery tests also show the same behavior regarding the RH effect. Figures 15 and 16 display stress-time and strain-time curves considering 50% of F_{ult} and 70% of F_{ult}, respectively. Since the ultimate force level is reduced by increasing the relative humidity level (Figures 12 to 14), the corresponding stress in the creep-recovery tests is also reduced, as expected (Figure 15-a and 16-a). The strain in the creep-recovery test depends on both the corresponding stress and RH level. Figure 15-b shows no trend in terms of total strain and plastic strain when the creep loading level is 50% of F_{ult}. However, when the creep loading level is 70% of F_{ult}, the plastic strain increases by increasing RH. The maximum total strain level also increases by increasing RH, except for RH80 which is at the same level as RH65. This means that the effect of RH is more pronounced than the effect of the stress level in the creep-recovery results with 70% of F_{ult}. The effect of both stress level and RH can be also observed together in the stress-strain curves in Figures 17 and 18. Loading-unloading mechanical responses are plotted as stress-strain curves and depicted in Figure 19. As observed, increasing RH decreases the stress level, as expected. In the following section, the stress and strain values obtained from the present mechanical tests are used to identify the model parameters at different RH levels.

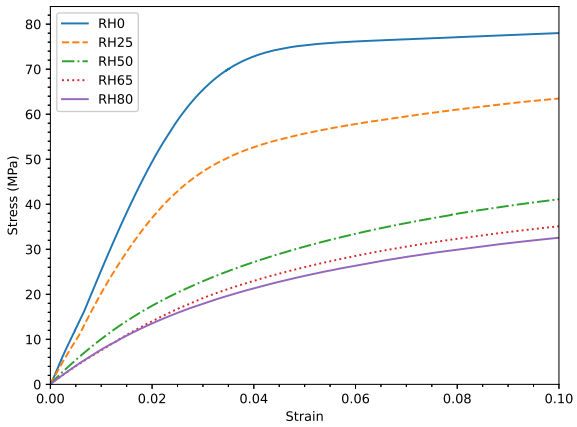

Figure 12: Stress-strain curves obtained from monotonic tensile tests performed on the dog bone samples at 4 × $10^{-4}\,s^{-1}$ strain rate.

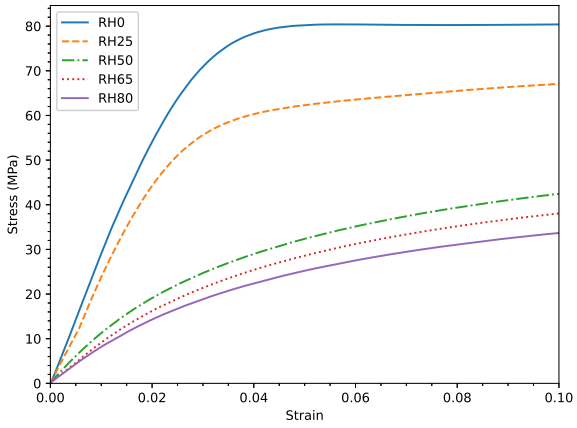

Figure 13: Stress-strain curves obtained from monotonic tensile tests performed on the dog bone samples at 4 × $10^{-3}\,s^{-1}$ strain rate.

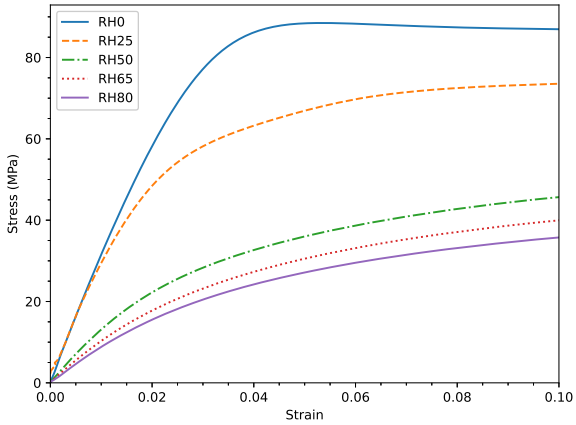

Figure 14: Stress-strain curves obtained from monotonic tensile tests performed on the dog bone samples at $4 \times 10^{-2}\,\mathrm{s}^{-1}$ strain rate.

Table 4: Polyamide 66 mechanical behavior versus RH and glass transition temperature (the values are extracted from Figure 3).

RH (%)	T_g (^{o}C)	$T - T_g$ (^{o}C)	Material behavior
0	75	-50	glassy state
25	60	-35	glassy state
50	25	0	viscoelastic (VE)
65	17	8	VE, mostly rubbery state
80	5	20	VE, mostly rubbery state

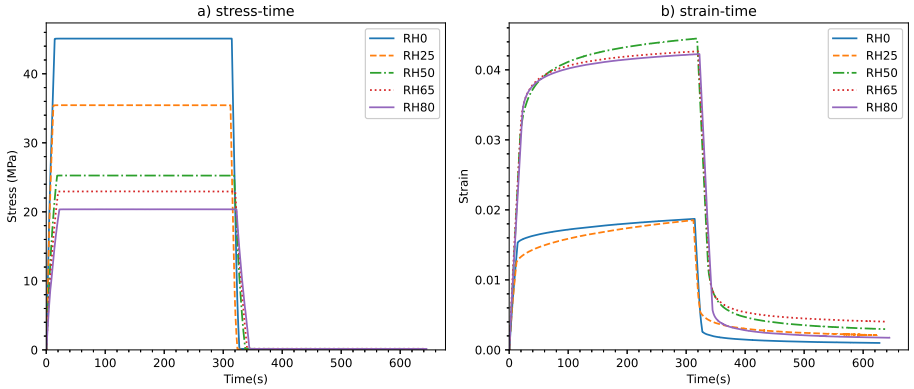

Figure 15: Stress-time and strain-time curves obtained from creep-recovery tests at different RH levels with 4 × $10^{-3}\,s^{-1}$ strain rate and 50% of F_{max}.

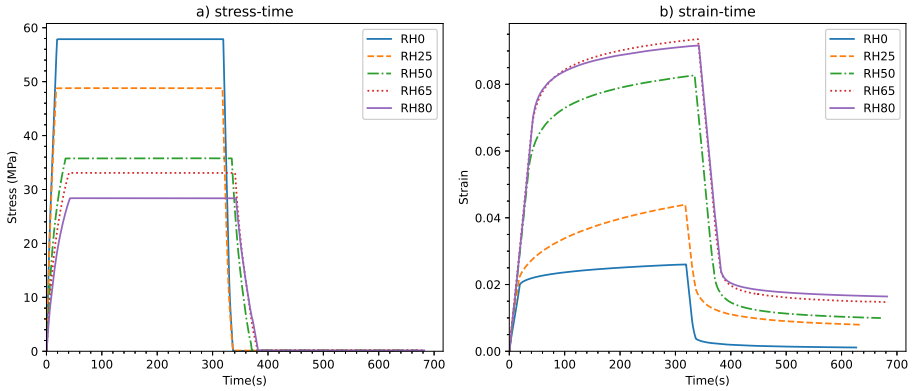

Figure 16: Stress-time and strain-time curves obtained from creep-recovery tests at different RH levels with 4 × $10^{-3}\,s^{-1}$ strain rate and 70% of F_{max}.

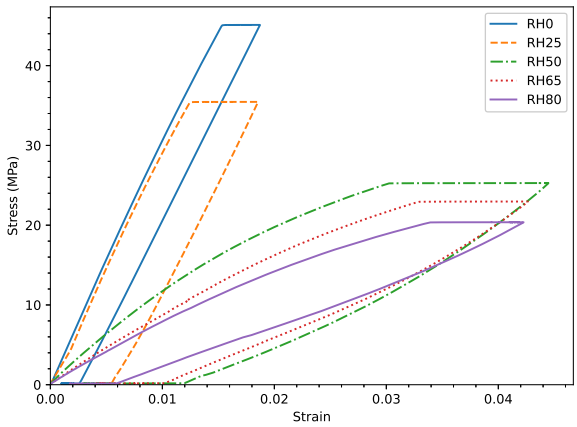

Figure 17: Stress-strain curves of creep-recovery tests at different RH levels with $4 \times 10^{-3}\,\mathrm{s}^{-1}$ strain rate and 50% of F_{ult}.

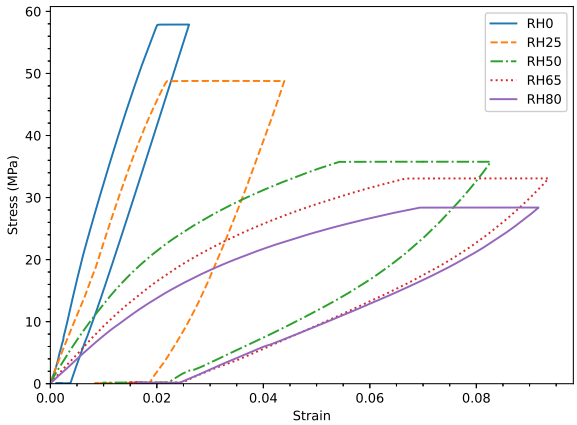

Figure 18: Stress-strain curves of creep-recovery tests at different RH levels with $4 \times 10^{-3}\,\mathrm{s}^{-1}$ strain rate and 70% of F_{ult}.

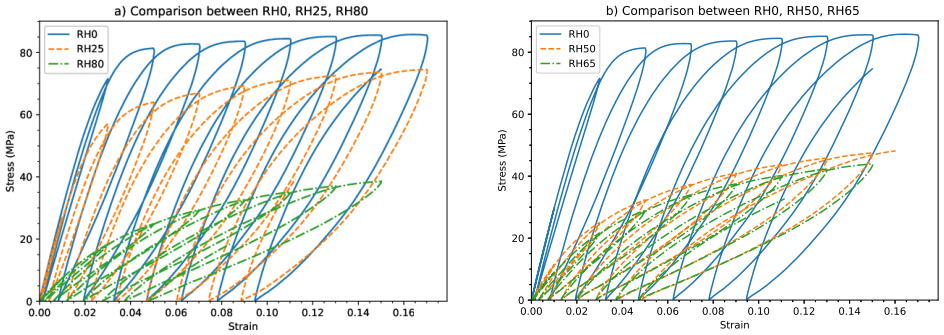

Figure 19: Stress-strain curves of loading-unloading test with increasing strain when the strain rate is $4 \times 10^{-3}\,\mathrm{s}^{-1}$.

3.4. Model calibration

A 0D homemade solver is used to produce numerical data for the calibration algorithm, in which, the difference between the experimental and numerical variables (stress or strain depending on the loading conditions) is minimized to find the appropriate parameters for the model at the corresponding RH level. To this end, the cost function between the experimental and numerical results is formed as a multidimensional function based on the model parameters, and Nelder-Mead method is used to find the appropriate set of parameters minimizing it. Nelder-Mead approach operates directly by comparing the function values and does not rely on the derivatives. In this method, for an n-dimensional function, a geometrical shape called "simplex" consisting of $n+1$ vertices is defined in an n-dimensional domain, as $\mathbb{R}^n$, and each vertex represents a set of parameters. For example, for $n = 2$, the "simplex" is a triangle, for $n = 3$, the "simplex" is a tetrahedron, etc. After determining the initial simplex, at each iteration, the value of the cost function at each vertex is computed, then the cost function values are sorted and replaced by new values calculated using the steps defined by the algorithm. This process continues until the standard deviation of the function values at the simplex vertices gets close to zero as much as possible. More details about the algorithm and its formulations are given in Nelder and Mead (1965); Singer and Nelder (2009). In this study, Nelder-Mead numerical approach is used through a Python standard library.

Figures 20 to 34 show the comparison between the calibrated numerical results and the experimental data. As observed, in the calibration procedure, it is tried to conduct the numerical results as close as possible to the experimental responses. However, the errors are relatively larger in the

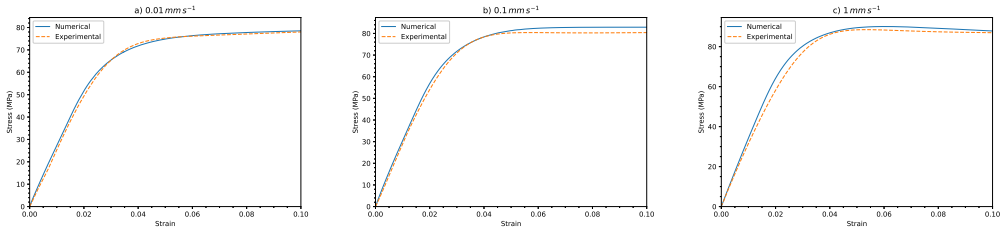

Figure 20: Calibration results for monotonic tests at RH0 under different displacement rates: a) $0.01\,\mathrm{mm\,s^{-1}}$, b) $0.1\,\mathrm{mm\,s^{-1}}$, c) $1\,\mathrm{mm\,s^{-1}}$.

monotonic test with the highest displacement rate ($1\,\mathrm{mm\,s^{-1}}$), particularly at RH50 and RH65. Furthermore, in the loading-unloading tests (Figures 22, 25, 28, 31, and 34), the experimental data show that the model captures accurately the elastic regime at the first loading-unloading cycles. At subsequent cycles the experimental results exhibit opening of the hysteresis loops due to the thermal softening. The latter is not accounted for in the model, which gives smaller hysterisis loops. A fully coupled thermo-mechanical model, in which the coupling between temperature and inelastic mechanisms is accounted for, can partially capture this opening of the hysterisis loops (Felder et al., 2020). The obtained identified parameters are listed in Table 5 and plotted with respect to RH as shown in Figure 35. As seen, the viscoelastic moduli have an approximately decreasing trend by an increase in RH except E^{v4} which increases. Some of the viscoplastic and damage-related parameters, H_p, R_{vp}, P_{vp}, and β_D can be fitted with increasing or decreasing trend lines. However, H_m, S_D, and R_0 do not follow any certain increasing or decreasing trend.

3.5. Model validation

As indicated before, the validation of the model presented in the previous sections is implemented through stepped creep-recovery, cyclic, and loading-unloading tests in the small deformation zone (less than 10%), and the results are plotted and shown in Figures 36 to 40. For RH0, the creep-recovery numerical simulation is in a good agreement with the experimental data for 50% and 70% of F_{ult} (Figure 36-a). At 90% of F_{ult}, the model predictions deviate from the experimental findings. Also, for the cyclic test at RH0, the numerical response loops are more inclined than the experimental data, which means that the damage is overestimated in the model (Figure 36-b). For the loading-unloading test at RH0, the model generally provides a good agreement with the

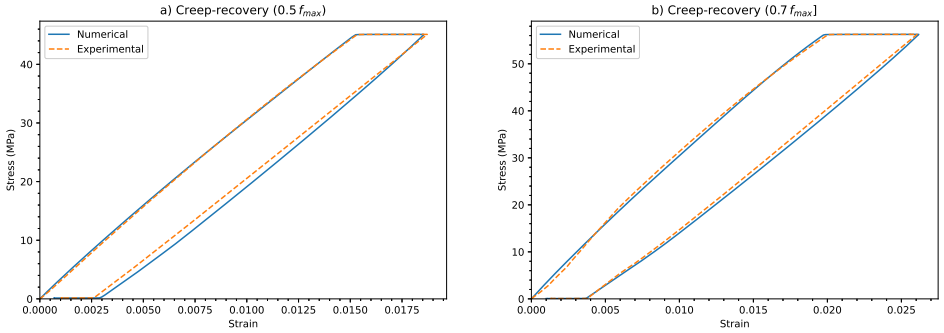

Figure 21: Calibration results for creep-recovery tests at RH0 under different loading levels: a) 50% of F_{ult}, b) 70% of F_{ult}.

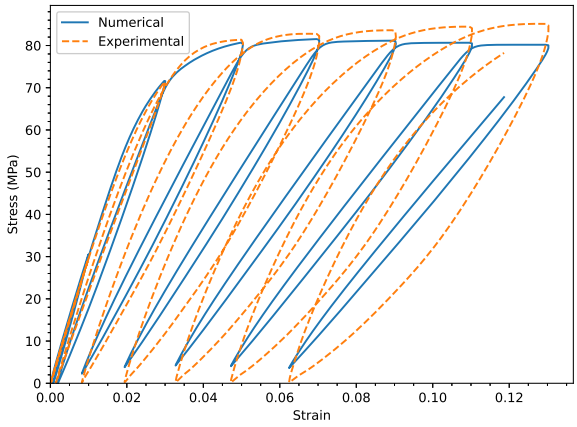

Figure 22: Calibration results for loading-unloading test at RH0.

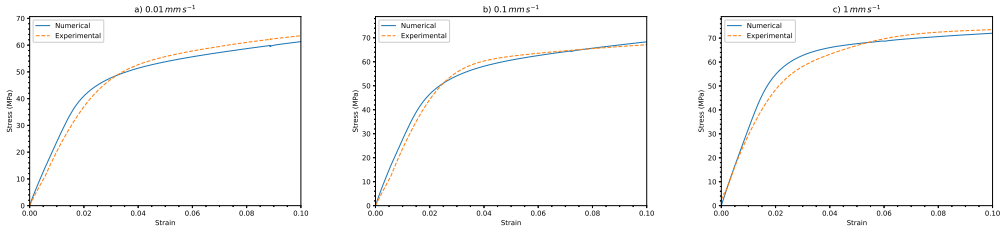

Figure 23: Calibration results for monotonic tests at RH25 under different displacement rates: a) $0.01\,\mathrm{mm\,s^{-1}}$, b) $0.1\,\mathrm{mm\,s^{-1}}$, c) $1\,\mathrm{mm\,s^{-1}}$.

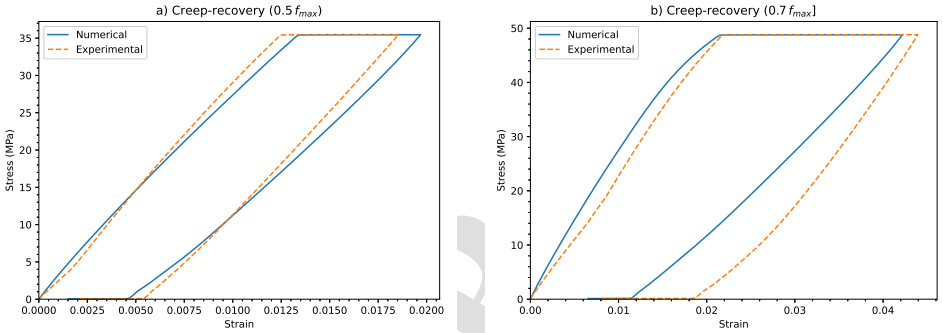

Figure 24: Calibration results for creep-recovery tests at RH25 under different loading levels: a) 50% of F_{ult}, b) 70% of F_{ult}.

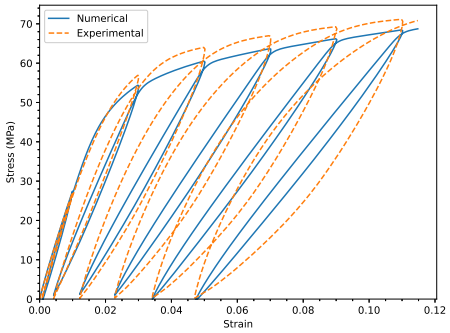

Figure 25: Calibration results for loading-unloading test at RH25.

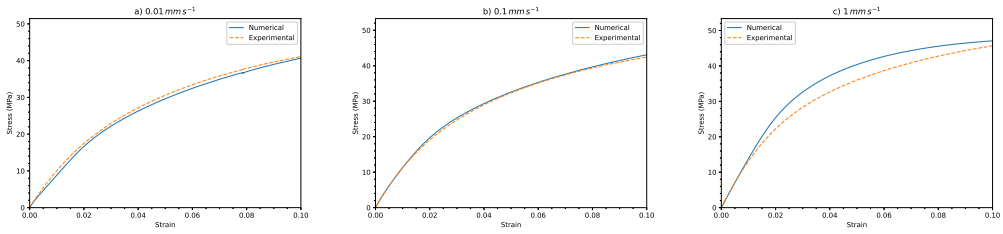

Figure 26: Calibration results for monotonic tests at RH50 under different displacement rates: a) $0.01\,\mathrm{mm\,s^{-1}}$, b) $0.1\,\mathrm{mm\,s^{-1}}$, c) $1\,\mathrm{mm\,s^{-1}}$.

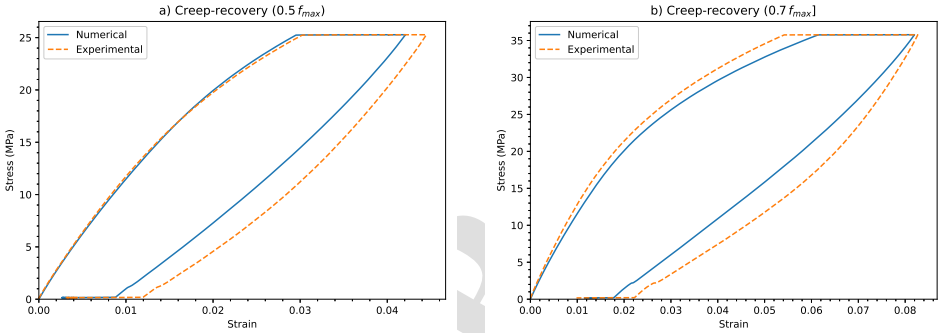

Figure 27: Calibration results for creep-recovery tests at RH50 under different loading levels: a) 50% of F_{ult}, b) 70% of F_{ult}.

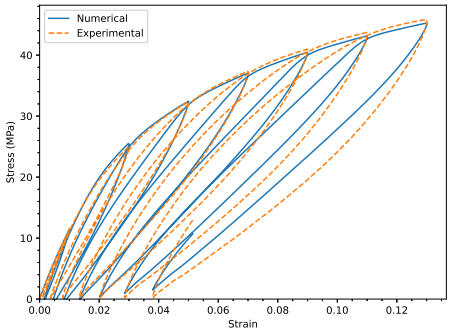

Figure 28: Calibration results for loading-unloading test at RH50.

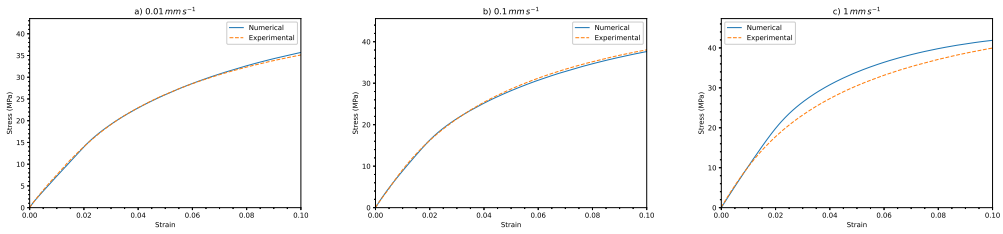

Figure 29: Calibration results for monotonic tests at RH65 under different displacement rates: a) $0.01\,\mathrm{mm\,s^{-1}}$, b) $0.1\,\mathrm{mm\,s^{-1}}$, c) $1\,\mathrm{mm\,s^{-1}}$.

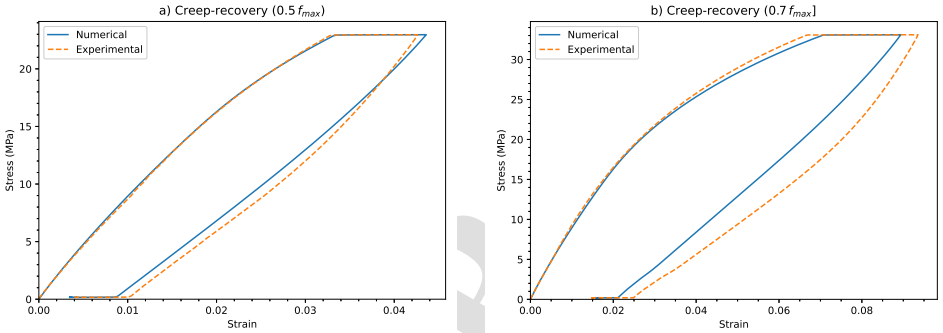

Figure 30: Calibration results for creep-recovery tests at RH65 under different loading levels: a) 50% of F_{ult}, b) 70% of F_{ult}.

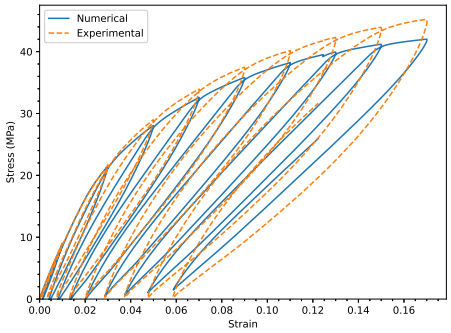

Figure 31: Calibration results for loading-unloading test at RH65.

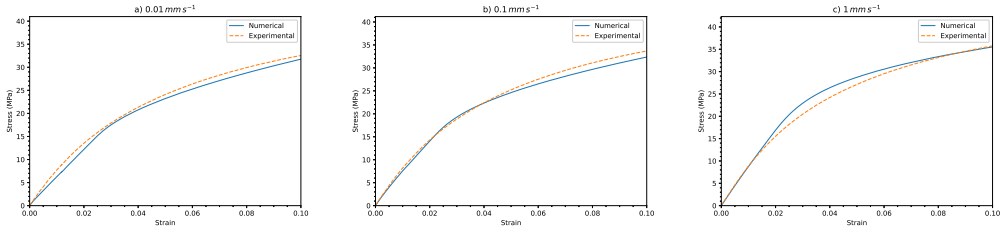

Figure 32: Calibration results for monotonic tests at RH80 under different displacement rates: a) $0.01\,\mathrm{mm\,s^{-1}}$, b) $0.1\,\mathrm{mm\,s^{-1}}$, c) $1\,\mathrm{mm\,s^{-1}}$.

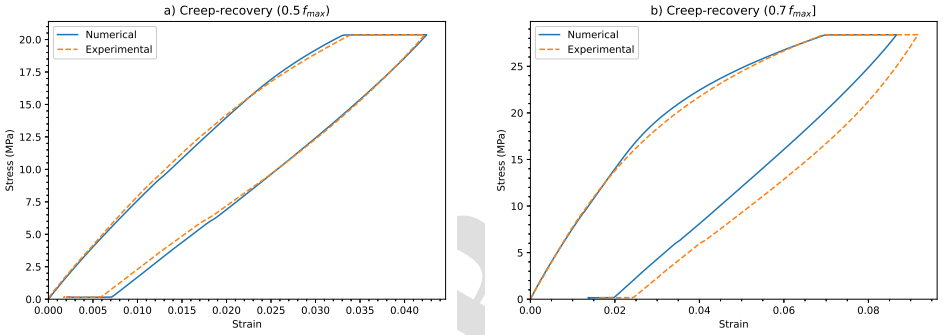

Figure 33: Calibration results for creep-recovery tests at RH80 under different loading levels: a) 50% of F_{ult}, b) 70% of F_{ult}.

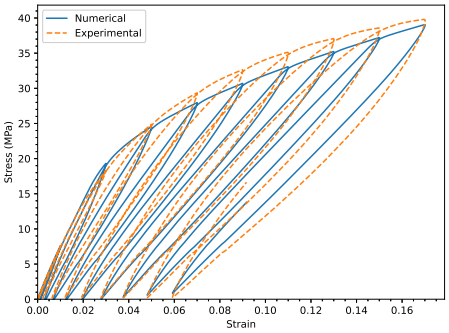

Figure 34: Calibration results for loading-unloading test at RH80.

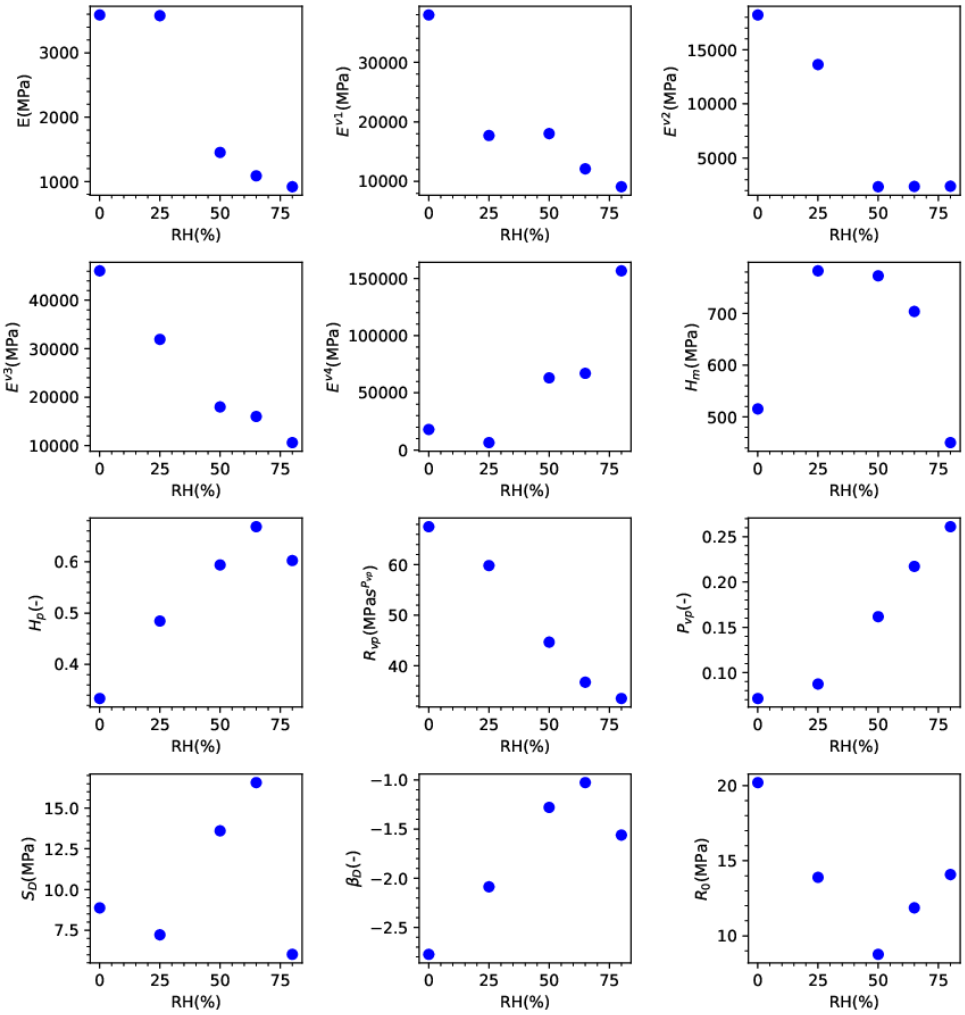

Figure 35: Identified model parameters variation with respect to RH.

Table 5: Calibrated model parameters at different RH levels.

Parameters	RH0	RH25	RH50	RH65	RH80
E (MPa)	3588.99	3577.91	1452.46	1088.50	918.80
E^{v1} (MPa)	37935.58	17702.06	18025.02	12116.62	9104.26
E^{v2} (MPa)	18202.36	13626.63	2350.54	2375.67	2400.77
E^{v3} (MPa)	46065.55	31916.05	17975.70	16002.66	10611.56
E^{V4} (MPa)	17947.79	6454.42	63073.45	67036.98	156679.06
H_m (MPa)	515.40	782.34	772.68	703.76	450.21
H_p $(-)$	0.33	0.48	0.59	0.67	0.60
R_{vp}(MPa.s$^{P_{vp}}$)	67.52	59.83	44.67	36.73	33.51
P_{vp} $(-)$	0.07	0.09	0.16	0.22	0.26
S_D (MPa)	8.87	7.22	13.60	16.57	6.02
β_D $(-)$	-2.77	-2.09	-1.28	-1.02	-1.56
R_0 (MPa)	20.20	13.89	8.77	11.86	14.08

experimental data, however, the loading-unloading loops obtained from the model are smaller than those from the experiment (Figure 36-c). Similarly, for the creep-recovery test at RH25, the model response is not well validated relatively at 90% of F_{ult} (Figure 37-a), and the cyclic test loops are more inclined (Figure 37-b). Moreover, for the cyclic test, it is observed that the loops obtained from the model are smaller than those from the experimental data (Figure 37-b). As observed, the results are better validated when RH is more than or equal to 50%. However, the numerical results are closer to the experimental data for RH50 and RH65 (Figures 38 and 39). For RH80, as seen in Figure 40-b, the cyclic test loops obtained from the model are slightly more inclined than those from the experiment. The latter indicates that the sample is less damaged than the model predicts, as also observed at RH0 and RH25. These differences in the validation results stem from the effect of the glass transition temperature, and the fact that the material behaves as mostly glassy at low RH and mostly rubbery at high RH. To account for such effects, the model may need to consider brittle damage or fewer viscoelastic branches at low RH and more viscoelastic branches at high RH. However, the objective of this study is to investigate the effect of humidity on the model parameters using a constant number of viscoelastic branches and characteristic times.

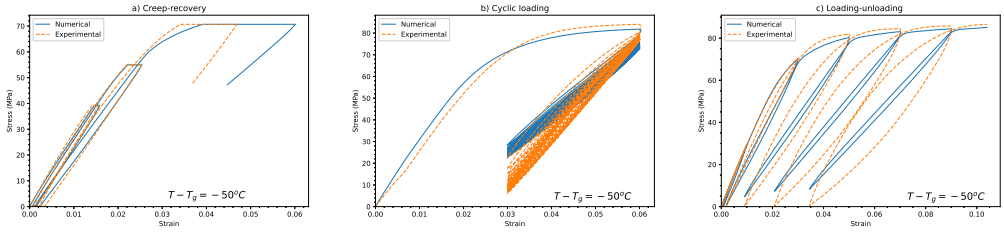

Figure 36: Validation results at RH0: a) creep-recovery test with $0.01\,\mathrm{mm\,s^{-1}}$ displacement rate, b) cyclic loading with $0.1\,\mathrm{mm\,s^{-1}}$ displacement rate, c) loading-unloading with $0.05\,\mathrm{mm\,s^{-1}}$ displacement rate.

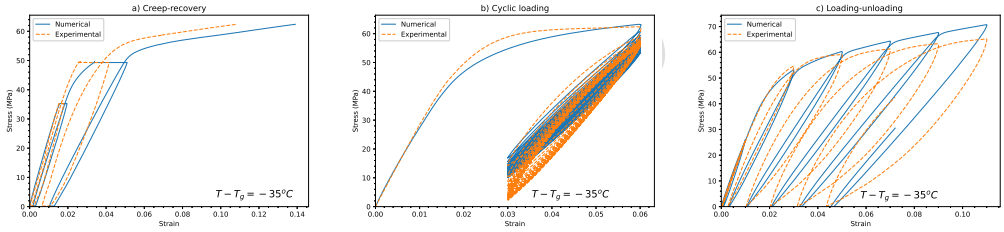

Figure 37: Validation results at RH25: a) creep-recovery test with $0.01\,\mathrm{mm\,s^{-1}}$ displacement rate, b) cyclic loading with $0.1\,\mathrm{mm\,s^{-1}}$ displacement rate, c) loading-unloading with $0.05\,\mathrm{mm\,s^{-1}}$ displacement rate.

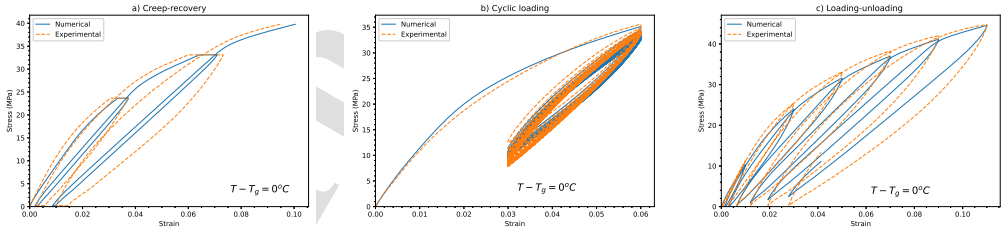

Figure 38: Validation results at RH50: a) creep-recovery test with $0.01\,\mathrm{mm\,s^{-1}}$ displacement rate, b) cyclic loading with $0.1\,\mathrm{mm\,s^{-1}}$ displacement rate, c) loading-unloading with $0.05\,\mathrm{mm\,s^{-1}}$ displacement rate.

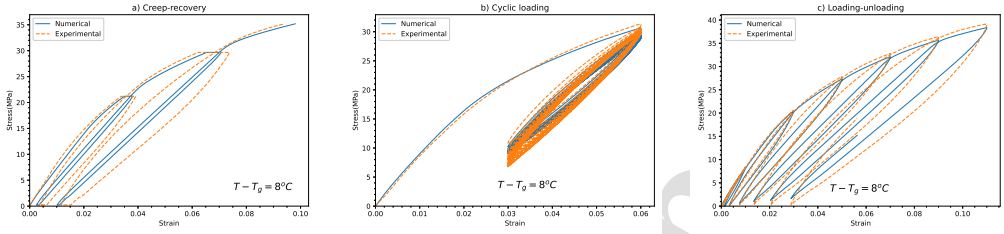

Figure 39: Validation results at RH65: a) creep-recovery test with $0.01\,\mathrm{mm\,s^{-1}}$ displacement rate, b) cyclic loading with $0.1\,\mathrm{mm\,s^{-1}}$ displacement rate, c) loading-unloading with $0.05\,\mathrm{mm\,s^{-1}}$ displacement rate.

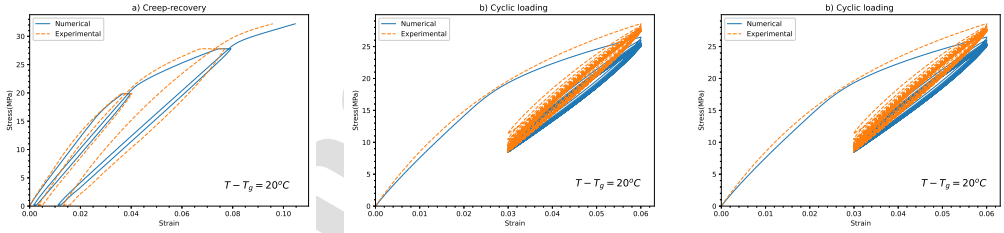

Figure 40: Validation results at RH80: a) creep-recovery test with $0.01\,\mathrm{mm\,s^{-1}}$ displacement rate, b) cyclic loading with $0.1\,\mathrm{mm\,s^{-1}}$ displacement rate, c) loading-unloading with $0.05\,\mathrm{mm\,s^{-1}}$ displacement rate.

4. Conclusions

In this research, an experimental method is presented to calibrate and validate the VEVPD model for polyamide 66, in which the change of dominant mechanisms from rubbery-like to glassy-like through moisture absorption is considered and studied. To calibrate the model, first the dog bone samples are conditioned at different RH levels. Then, considering the dominant active mechanisms, mechanical tests including monotonic, cyclic, and creep-recovery tests with several loading rates are implemented. The mechanical tests show that time-dependent strain along with creep and ductile damage depend on the sample water uptake represented by different RH conditioning levels. The effect of relative humidity on the model parameters is explored, which follows decreasing and increasing trends in the viscoelastic parameters. In this study, for the first time the VEVPD model is calibrated and validated for PA66 at different relative humidity levels, namely: RH0, RH25, RH65, and RH80. The validation results reveal that the VEVPD model provides accurate predictions for high RH level namely: RH50, RH65, RH80.

The validation tests reveal that the model captures less efficiently the experimental curves at RH0 and RH25. This suggests that the model does not capture properly certain active mechanisms at low RH, such as brittle damage or almost rate-independent response of thermoplastics at low extent of water content. This can be addressed by developing an elasto-viscoplastic model with brittle damage decoupled from plasticity (Brepols et al., 2017; Zaïri et al., 2007; Lemaitre and Chaboche, 1994). In the present work, the VEVPD model was calibrated for the pure polyamide 66, however the glass reinforced polyamide 66 has a large amount of applications in the industry under different operating conditions. The VEVPD model, for constant RH, has been already extended to the multi-scale frameworks through mean-field and full-field homogenization approaches depending on the fiber shapes and orientations (Barral et al., 2020; Chen et al., 2021; Tikarrouchine et al., 2021; Chen et al., 2022). A similar experimental approach can be implemented on the different types of polyamide 66 composites to evaluate efficiency of the multi-scale models at different RH level. To predict the long-term mechanical responses of polyamide 66 and glass reinforced polyamide 66, other environmental factors must be considered based on operating conditions, such as contact with chemical solvents, exposure to high or low temperatures, etc. For example, glass-reinforced thermoplastics used in the automotive industry are in permanent contact with chemical solvents, such as antifreeze (a mixture of water and ethylene glycol), which affects their mechanical behavior, and the nonlinear inelastic mechanisms are strongly affected, resulting in glassy to rubbery

and less or more time-dependent behavior (Pires, 2000; Chekkour et al., 2023). These operating conditions are often along with high temperature, such as the composites used in the cooling radiators (Ledieu, 2010). Thus, further extensions of the model could include more environmental factors and incorporate to chemico-mechanical couplings.

Acknowledgement

This work has been carried out in the framework of the THERMOFIP project (FUI-BPI project) led by DOMO Chemicals. The authors are grateful to DOMO Chemicals for supporting this work, providing the test material, and sharing knowledge and practical tips that allowed the improvement of the humidity conditioning procedure.

References

Apinis A, Galvanovskii AY, et al. The effect of the moisture content on the transition temperatures of polycaproamide. Polymer Science USSR 1975;17(1):46–51. doi:10.1016/0032-3950(75)90212-9.

Arhant M, Le Gac PY, Le Gall M, Burtin C, Briançon C, Davies P. Modelling the non fickian water absorption in polyamide 6. Polymer Degradation and Stability 2016;133:404–12. doi:10.1016/j.polymdegradstab.2016.09.001.

Arif M, Meraghni F, Chemisky Y, Despringre N, Robert G. In situ damage mechanisms investigation of PA66/GF30 composite: Effect of relative humidity. Composites Part B: Engineering 2014a;58:487 – 495. doi:10.1016/j.compositesb.2013.11.001.

Arif M, Saintier N, Meraghni F, Fitoussi J, Chemisky Y, Robert G. Multiscale fatigue damage characterization in short glass fiber reinforced polyamide-66. Composites Part B: Engineering 2014b;61:55–65. doi:10.1016/j.compositesb.2014.01.019.

Arruda E, Boyce M. A three-dimensional constitutive model for the large stretch behavior of rubber elastic materials. Journal of The Mechanics and Physics of Solids 1993;41(2):389–412. doi:10.1016/0022-5096(93)90013-6.

Arruda EM, Boyce MC, Jayachandran R. Effects of strain rate, temperature and thermomechanical coupling on the finite strain deformation of glassy polymers. Mechanics of Materials 1995;19(2-3):193–212. doi:10.1016/0167-6636(94)00034-e.

Barral M, Chatzigeorgiou G, Meraghni F, Léon R. Homogenization using modified Mori-Tanaka and TFA framework for elastoplastic-viscoelastic-viscoplastic composites: theory and numerical validation. International Journal of Plasticity 2020;127:102632. doi:10.1016/j.ijplas.2019.11.011.

Barrett RA, O'Donoghue P, Leen SB. An improved unified viscoplastic constitutive model for strain-rate sensitivity in high temperature fatigue. International Journal of Fatigue 2013;48:192–204. doi:10.1016/j.ijfatigue.2012.11.001.

Bellenger V, Tcharkhtchi A, Castaing P. Thermal and mechanical fatigue of a PA66/glass fibers composite material. International journal of Fatigue 2006;28(10):1348–52. doi:10.1016/j.ijfatigue.2006.02.031.

Benaarbia A, Chatzigeorgiou G, Kiefer B, Meraghni F. A fully coupled thermo-viscoelastic-viscoplastic-damage framework to study the cyclic variability of the Taylor-Quinney coefficient for semi-crystalline polymers. International Journal of Mechanical Sciences 2019;163:105128. doi:10.1016/j.ijmecsci.2019.105128.

Benaarbia A, Chrysochoos A, Robert G. Kinetics of stored and dissipated energies associated with cyclic loadings of dry polyamide 6.6 specimens. Polymer Testing 2014;34:155–67. doi:10.1016/j.polymertesting.2014.01.009.

Benaarbia A, Chrysochoos A, Robert G. Thermomechanical analysis of the onset of strain concentration zones in wet polyamide 6.6 subjected to cyclic loading. Mechanics of Materials 2016;99:9–25. doi:10.1016/j.mechmat.2016.04.011.

Benaarbia A, Rae Y, Sun W. Unified viscoplasticity modelling and its application to fatigue-creep behaviour of gas turbine rotor. International Journal of Mechanical Sciences 2018a;136:36–49. doi:10.1016/j.ijmecsci.2017.12.008.

Benaarbia A, Rouse JP, Sun W. A thermodynamically-based viscoelastic-viscoplastic model for

the high temperature cyclic behaviour of 9-12% Cr steels. International Journal of Plasticity 2018b;107:100–21. doi:10.1016/j.ijplas.2018.03.015.

Bergeret A, Pires I, Foulc M, Abadie B, Ferry L, Crespy A. The hygrothermal behaviour of glass-fibre-reinforced thermoplastic composites: a prediction of the composite lifetime. Polymer testing 2001;20(7):753–63. doi:10.1016/s0142-9418(01)00030-7.

Billon N. New constitutive modeling for time-dependent mechanical behavior of polymers close to glass transition: Fundamentals and experimental validation. Journal of Applied Polymer Science 2012;125(6):4390–401. doi:10.1002/app.36598.

Brepols T, Wulfinghoff S, Reese S. Gradient-extended two-surface damage-plasticity: Micromorphic formulation and numerical aspects. International Journal of Plasticity 2017;97:64–106. doi:10.1016/j.ijplas.2017.05.010.

Broudin M, Le Gac PY, Le Saux V, Champy C, Robert G, Charrier P, Marco Y. Water diffusivity in PA66: Experimental characterization and modeling based on free volume theory. European Polymer Journal 2015;67:326–34. doi:10.1016/j.eurpolymj.2015.04.015.

Brydson J. Polyamides and polyimides. Butterworth-Heinemann Oxford, 1999. doi:10.1016/b978-075064132-6/50059-0.

Cailletaud G, Sai K. Study of plastic/viscoplastic models with various inelastic mechanisms. International Journal of Plasticity 1995;11(8):991–1005. doi:10.1016/s0749-6419(95)00040-2.

Carrascal I, Casado J, Polanco J, Gutiérrez-Solana F. Absorption and diffusion of humidity in fiber glass-reinforced polyamide. Polymer composites 2005;26(5):580–6. doi:10.1002/pc.20134.

Chaboche JL. Thermodynamic formulation of constitutive equations and application to the viscoplasticity and viscoelasticity of metals and polymers. International Journal of Solids and Structures 1997;34(18):2239–54. doi:10.1016/s0020-7683(96)00162-x.

Chaboche JL. A review of some plasticity and viscoplasticity constitutive theories. International Journal of Plasticity 2008;24(10):1642–93. doi:10.1016/j.ijplas.2008.03.009.

Chaboche JL, Rousselier G. On the plastic and viscoplastic constitutive equations—part I: rules developed with internal variable concept. Journal of Pressure Vessel Technology 1983;doi:10.1115/1.3264257.

Chekkour R, Benaarbia A, Chatzigeorgiou G, Meraghni F, Robert G. Effect of thermo-hygro glycol aging on the damage mechanisms of short glass-fiber reinforced polyamide 66. Composites Part A: Applied Science and Manufacturing 2023;165:107358. doi:10.1016/j.compositesa.2022.107358.

Chen Q, Chatzigeorgiou G, Meraghni F. Extended mean-field homogenization of viscoelastic-viscoplastic polymer composites undergoing hybrid progressive degradation induced by interface debonding and matrix ductile damage. International Journal of Solids and Structures 2021;210:1–17. doi:10.1016/j.ijsolstr.2020.11.017.

Chen Q, Chatzigeorgiou G, Robert G, Meraghni F. Viscoelastic-viscoplastic homogenization of short glass-fiber reinforced polyamide composites (PA66/GF) with progressive interphase and matrix damage: New developments and experimental validation. Mechanics of Materials 2022;164:104081. doi:10.1016/j.mechmat.2021.104081.

Chen Q, Chatzigeorgiou G, Robert G, Meraghni F. Combination of mean-field micromechanics and cycle jump technique for cyclic response of PA66/GF composites with viscoelastic-viscoplastic and damage mechanisms. Acta Mechanica 2023;234:1533–52. doi:10.1007/s00707-022-03448-4.

Contesti E, Cailletaud G. Description of creep-plasticity interaction with non-unified constitutive equations: application to an austenitic stainless steel. Nuclear engineering and design 1989;116(3):265–80. doi:10.1016/0029-5493(89)90087-3.

Detrez F, Cantournet S, Seguela R. Plasticity/damage coupling in semi-crystalline polymers prior to yielding: Micromechanisms and damage law identification. Polymer 2011;52(9):1998–2008. doi:10.1016/j.polymer.2011.03.012.

Felder S, Holthusen H, Hesseler S, Pohlkemper F, Gries T, Simon JW, Reese S. Incorporating crystallinity distributions into a thermo-mechanically coupled constitutive model for semi-crystalline polymers. International Journal of Plasticity 2020;135:102751.

Germain P, Suquet P, Nguyen QS. Continuum thermodynamics. ASME Journal of Applied Mechanics 1983;50:1010–20. doi:10.1115/1.3167184.

Halphen B, Nguyen QS. Sur les matériaux standard généralisés. Journal de mécanique 1975;14(1):39–63.

Ishisaka A, , Kawagoe M. Examination of the time–water content superposition on the dynamic viscoelasticity of moistened polyamide 6 and epoxy. Journal of Applied Polymer Science 2004;93(2):560–7. doi:10.1002/app.20465.

Kachanov L. Time of the rupture process under creep conditions. Izvestiia akademii nauk sssr, otdelenie teckhnicheskikh nauk 1958;8:26–31.

Kang G, Kan Q. Constitutive modeling for uniaxial time-dependent ratcheting of ss304 stainless steel. Mechanics of Materials 2007;39(5):488–99. doi:10.1016/j.mechmat.2006.08.004.

Kauffman GB. Wallace hume carothers and nylon, the first completely synthetic fiber. Journal of Chemical Education 1988;65(9):803. doi:10.1021/ed065p803.

Krairi A, Doghri I. A thermodynamically-based constitutive model for thermoplastic polymers coupling viscoelasticity, viscoplasticity and ductile damage. International Journal of Plasticity 2014;60:163–81. doi:10.1016/j.ijplas.2014.04.010.

Launay A, Maitournam M, Marco Y, Raoult I, Szmytka F. Cyclic behaviour of short glass fibre reinforced polyamide: Experimental study and constitutive equations. International Journal of Plasticity 2011;27(8):1267–93. doi:10.1016/j.ijplas.2011.02.005.

Launay A, Marco Y, Maitournam M, Raoult I. Modelling the influence of temperature and relative humidity on the time-dependent mechanical behaviour of a short glass fibre reinforced polyamide. Mechanics of Materials 2013;56:1–10. doi:10.1016/j.mechmat.2012.08.008.

Le Gac PY, Arhant M, Le Gall M, Davies P. Yield stress changes induced by water in polyamide 6: Characterization and modeling. Polymer Degradation and Stability 2017;137:272–80. doi:10.1016/j.polymdegradstab.2017.02.003.

Ledieu B. Vieillissement en milieu eau/glycol du polyamide 66 renforce fibres de verre courtes pour l'application boite a eau de radiateur de refroidissement moteur. Ph.D. thesis; Arts et Métiers ParisTech; 2010.

Lemaitre J, Chaboche J. Mechanics of solid materials. Cambridge university press, 1994.

Miled B, Doghri I, Delannay L. Coupled viscoelastic-viscoplastic modeling of homogeneous and isotropic polymers: Numerical algorithm and analytical solutions. Computer methods in applied mechanics and engineering 2011;200(47-48):3381–94. doi:10.1016/j.cma.2011.08.015.

Nelder JA, Mead R. A simplex method for function minimization. The computer journal 1965;7(4):308–13. doi:10.1093/comjnl/7.4.308.

Obeid H. Durabilité de composites à matrice thermoplastique sous chargement hygro-mécanique: étude multi-physique et multi-échelle des relations microstructure-propriétés-états mécaniques. Ph.D. thesis; Nantes; 2016.

Obeid H, Clément A, Fréour S, Jacquemin F, Casari P. On the identification of the coefficient of moisture expansion of polyamide-6: Accounting differential swelling strains and plasticization. Mechanics of Materials 2018;118:1–10. doi:10.1016/j.mechmat.2017.12.002.

Parodi E, Peters GW, Govaert LE. Prediction of plasticity-controlled failure in polyamide 6: Influence of temperature and relative humidity. Journal of Applied Polymer Science 2018;135(11):45942.

Pipkin A, Rogers T. A non-linear integral representation for viscoelastic behaviour. Journal of the Mechanics and Physics of Solids 1968;16(1):59–72. doi:10.1016/0022-5096(68)90016-1.

Pires I. Vieillissement dans l'antigel de matériaux composites polyamide-6, 6 renforcé par des fibres de verre courtes. Ph.D. thesis; Montpellier 2; 2000.

Pivdiablyk I, Rozycki P, Jacquemin F, Gornet L, Auger S. Experimental analysis of mechanical performance of glass fibre reinforced polyamide 6 under varying environmental conditions. Composite Structures 2020;245:112338. doi:10.1016/j.compstruct.2020.112338.

Post N, Riebel F, Zhou A, Keller T, Case S, Lesko J. Investigation of 3D moisture diffusion coefficients and damage in a pultruded E-glass/polyester structural composite. Journal of composite materials 2009;43(1):75–96.

Pramoda K, Liu T. Effect of moisture on the dynamic mechanical relaxation of polyamide-6/clay nanocomposites. Journal of Polymer Science Part B: Polymer Physics 2004;42(10):1823–30. doi:10.1002/polb.20061.

Praud F, Chatzigeorgiou G, Bikard J, Meraghni F. Phenomenological multi-mechanisms constitutive modelling for thermoplastic polymers, implicit implementation and experimental validation. Mechanics of Materials 2017;114:9–29. doi:10.1016/j.mechmat.2017.07.001.

Rabotnov Y. Creep rupture. Springer Berlin Heidelberg, 1968. doi:10.1007/978-3-642-85640-2_26.

Reimschuessel H. Relationships on the effect of water on glass transition temperature and Young's modulus of Nylon 6. Journal of Polymer Science: Polymer Chemistry Edition 1978;16(6):1229–36. doi:10.1002/pol.1978.170160606.

Rivlin R. Integral representations of constitutive equations. Rheologica Acta 1983;22(3):260–7. doi:10.1007/978-1-4612-2416-7_101.

Sambale A, Kurkowski M, Stommel M. Determination of moisture gradients in polyamide 6 using stepscan DSC. Thermochimica Acta 2019;672:150–6. doi:10.1016/j.tca.2018.12.011.

Singer S, Nelder J. Nelder-Mead algorithm. Scholarpedia 2009;4(7):2928. doi:10.4249/scholarpedia.2928; revision #91557.

Tikarrouchine E, Benaarbia A, Chatzigeorgiou G, Meraghni F. Non-linear FE2 multiscale simulation of damage, micro and macroscopic strains in polyamide 66-woven composite structures: analysis and experimental validation. Composite Structures 2021;255:112926. doi:10.1016/j.compstruct.2020.112926.

Velay V, Bernhart G, Penazzi L. Cyclic behavior modeling of a tempered martensitic hot work tool steel. International Journal of Plasticity 2006;22(3):459–96. doi:10.1016/j.ijplas.2005.03.007.

Venoor V, Park JH, Kazmer DO, Sobkowicz MJ. Understanding the effect of water in polyamides: a review. Polymer Reviews 2021;61(3):598–645.

Vidinha H, Branco R, Neto MA, Amaro AM, Reis P. Numerical modeling of damage caused by seawater exposure on mechanical strength in fiber-reinforced polymer composites. Polymers 2022;14(19):3955. doi:10.3390/polym14193955.

Wang J, Gangarao H, Liang R, Liu W. Durability and prediction models of fiber-reinforced polymer composites under various environmental conditions: A critical review. Journal of Reinforced Plastics and Composites 2016;35(3):179–211.

Zaïri F, Naït-Abdelaziz M, Woznica K, Gloaguen JM. Elasto-viscoplastic constitutive equations for the description of glassy polymers behavior at constant strain rate. Journal of Engineering Materials and Technology 2007;129(1):29–35. doi:10.1115/1.2400256.

Zhang S, Huang Z, Zhang Y, Zhou H. Experimental investigation of moisture diffusion in short-glass-fiber-reinforced polyamide 6, 6. Journal of Applied Polymer Science 2015;132(37). doi:10.1002/app.42369.

Highlights

- The present model considers the effect of relative humidity (RH) on all inelastic mechanisms and ductile damage in polyamide (PA66).
- The model parameters are identified for RH=0%, 25%, 50%, 65%, and 80%, and the effect of RH on the model parameters, for the first time, is studied.
- An innovative experimental approach taking into account different loading conditions is designed to capture the various active mechanisms governing the nonlinear behavior of PA66.
- Validation of the model responses with experimental data under different levels of RH exposure and loading conditions indicates a good agreement between them.

AUTHORSHIP STATEMENT Manuscript title:

Numerical-experimental approach to identify the effect of relative humidity on the material parameters of a rate-dependent damage model for polyamide 66

Soheil Satouri: Writing - Original Draft, Formal Analysis, Investigation, Validation

Rabii Chekkour: Data curation, Formal Analysis, Investigation, Validation

George Chatzigeorgiou: Writing - Review & Editing, Methodology, Conceptualization, investigation

Fodil Meraghni: Conceptualization, Methodology, Writing - Review & Editing, Project administration

Gilles Robert: Resources, Data curation, Review & Editing,

Declaration of interests

☒ The authors declare that they have no known competing financial interests or personal relationships that could have appeared to influence the work reported in this paper.

☐The authors declare the following financial interests/personal relationships which may be considered as potential competing interests: